


Dynamics of Phase Fronts During High-Driving-Force Transformation of Shape Memory Alloy Wires

Asaf Dana¹  · Hiroshi Sekiguchi⁴ · Koki Aoyama⁴ · Eilon Faran¹ · Klaus-Dieter Liss^{2,3} · Doron Shilo¹

Received: 11 February 2021 / Revised: 19 April 2021 / Accepted: 19 April 2021 / Published online: 17 May 2021
© ASM International 2021

Abstract The reverse martensitic transformation proceeds through several sub-processes at various time and length scales. We recently studied the transformation kinetics in the large thermodynamic driving force regime. We induced a rapid heating pulse in a shape memory alloy wire and tracked its evolution by multi-frame time-resolved X-ray diffraction at synchrotron radiation with simultaneous stress measurements. The study identified three stages occurring at different times on the microsecond-scale and at different length scales. Specifically, the transformation was shown to occur initially in a thin layer near the surface, and only later in the bulk of the wire. Herein, we explain the obtained experimental results by modeling the evolution of the phase transformation using a continuum approach. Theoretical approaches are discussed and model fitting to experimental results provides insight into the kinetic relation between the velocity of the phase front and the driving force. Results support a scenario in which a cylindrical phase front propagates inward along the wire radius. The propagation of such a high-specific energy

front releases energy faster than low-energy fronts forming under low driving forces.

Keywords Large driving force · Phase front · Kinetic relations · NiTi · X-ray diffraction · Reverse martensitic transformation · Shape memory alloy · Synchrotron

Introduction

Martensitic transformations serve as the basic deformation mechanism in many functional materials. The question “how fast can the martensitic transformation be?” is elemental to the field of solid-solid phase transformations, e.g., [1, 2]. However, in most studies the transformation rate is restricted by heat or momentum transfer and the applied driving force is just slightly above the threshold value required for overcoming the transformation barriers.

The martensitic transformation occurs through several stages at different times and length scales. These stages have been thoroughly studied at slow ($\sim 10^{-4} \text{ s}^{-1}$) and intermediate ($\sim 1 \text{ s}^{-1}$) strain rates [3]. Yet, both cases are still in the small driving force regime. At slow rates, it was found that in polycrystalline materials, neighboring grains tend to transform in a coordinated manner that minimizes the strain incompatibility across grain boundaries [4]. Consequently, macroscopic phase fronts involving numerous grains are often observed [5]. At slow rates, these phase fronts are strain compatible at a scale much larger than the grain size [4].

The sequence of transformation stages and their characteristic times have not been thoroughly characterized in the large driving force regime. In many studies, a lack of experimental tools prevented tracking the evolution of the

✉ Asaf Dana
asafda@campus.technion.ac.il

Doron Shilo
shilo@technion.ac.il

¹ Department of Mechanical Engineering, Technion, Haifa 3200003, Israel

² Materials and Engineering Science Program, Guangdong Technion, Daxue Road, Jinping District, Guangdong 515063, Shantou, China

³ Technion, Haifa 3200003, Israel

⁴ Center for Synchrotron Radiation Research, Japan Synchrotron Radiation Research Institute, 1-1-1, Kouto, Sayo-cho, Hyogo, Sayo-gun, Japan

martensitic transformation with sufficient spatial and temporal resolutions. For example, high-rate impact tests in shape memory alloys (SMA) often lacked the ability to resolve discrete phase fronts [6, 7]. An investigation of a discrete phase front [8], tracked by a series of 9 strain gauges, displayed extensive data scattering. Thus, the kinetic relations between the thermodynamic driving force and the velocity of discrete phase fronts are currently unknown.

Recently, Vollach et al. [9–11] introduced a new experimental method for measuring the dynamic response of SMA wires subjected to an electric resistive Joule-heating pulse of a few microseconds. In these experiments, the temperature of the SMA wire reaches a constant value, above the austenite finish temperature, A_f , before the phase transformation begins. The wire was fixed at both ends, preventing motion of masses except for local motions in the wire, and the stress in the wire due to the phase transformation was measured. These experiments provide the desired conditions for measuring the unhindered kinetics of the transformation in the high driving force regime.

Previous Joule-heating pulse experiments were able to suggest a macro-scale kinetic law for the average stress in the wire as a function of time [9]. However, the lack of knowledge on the instantaneous volume fraction of the austenite prohibited the study of sub-processes of the phase transformation. In particular, the macro-scale stress measurement could not reveal a micro-scale kinetic relation for phase front propagation.

Quantitative information about the volume fractions of different phases can be obtained by time-resolved X-ray diffraction (XRD). Recent developments of extreme brilliant undulator X-ray sources enable capturing single [12] and multi-frame [13, 14] time-resolved diffraction patterns.

Dana et al. [15] combined the Joule-heating pulse experimental system with multi-frame time-resolved XRD to obtain local measures for the austenite volume fraction with a temporal resolution of 1 μ s. The results demonstrate the ability to obtain information on sub-processes at different time and length scales. Specifically, three different stages of the phase transformation were identified, occurring on the microsecond time scale. The transformation was shown to occur initially in a thin layer near the surface, and only later in the bulk of the wire.

Herein, we build on our experimental results reported in Ref. [15], and model the evolution of the phase transformation using a continuum approach. Namely, the dominant stage is hypothesized to occur via the propagation of a single phase front. The model predictions are in good agreement with experimental results and provide the kinetic relation of the phase front. The investigated phase

front is significantly different than all previously studied transformation phase fronts (see, e.g., Ref. [4]) for it is strain incompatible at the macroscopic scale. The misfit strains at the phase front induce internal stresses throughout the entire volume of the wire and increase the elastic energy. We show that this additional elastic energy is small with respect to the energy associated with the driving force for the transformation.

The Multi-frame Time-Resolved XRD Experiment

Materials and Methods

In this section, we briefly review the experimental details, presented in more details in Refs. [10, 15].

The martensite to austenite phase transformation was studied in a NiTi wire (Dynalloy Flexinol®90 °C, 50 at.%, $A_f \approx 80$ – 90 °C, with a grain size of approximately 100 nm) with a diameter of 0.2 mm. Flexinol is a preconditioned material that exhibits a two-way shape memory effect [10]. At room temperature, this material is completely at the martensite phase and the reverse martensitic transformations do not involve the formation of the intermediate R-phase. Initially, the NiTi wire was fixed at both ends under a constant tensile stress of $\sigma_0 = 200$ MPa. Under these conditions, the fully martensitic wire achieved a detwinned state with a transformation strain of approximately $\varepsilon_0 = 0.035$ relative to its original free length at the austenite phase. The fixed wire, initially at room temperature, was subjected to a rapid, high-voltage, electric pulse that heated it to a temperature in the range 433–473 K (160–200 °C, greater than A_f), during 3 μ s [10, 15]. Dedicated force sensors with a bandwidth of 1 MHz were attached to both ends of the NiTi wire and measured the force developed in the clamped wire throughout the experiment. Clamping the wire at both ends throughout the experiment assures that the transformation rate is unhindered by acceleration of masses.

Previous high-rate studies using IR imaging demonstrated that the temperature is uniform along the wire axis [10]. The characteristic penetration depth due to the electromagnetic skin effect is about 3 mm, indicating that for wires with a diameter of 0.2 mm the temperature change along the wire radius is smaller than 6 K [11]. Moreover, heat loss to the surrounding is shown to be negligible at the μ s time-scale, and the temperature is approximately constant during the entire duration of the phase transformation (see top panel in Fig. 3, as well as a detailed discussion of the temperature evolution in Ref. [15]).

Under a fixed wire length, the negative transformation strain is balanced by a positive elastic strain, associated

with an increase of the tensile stress. Thus, as the phase transformation proceeds the tensile stress increases, resulting in a decrease of the driving force for the transformation. Based on our previous work, under the described experimental conditions the phase transformation is not completed [15], and it is estimated that the transformed volume fraction does not exceed 0.3 [16, 17]. Thus, losses due to latent heat are smaller than 7 K [15]. The plastic strain after each pulse was validated to be negligible, as it did not exceed 10^{-3} , i.e., at least one order of magnitude smaller than the overall transformation strain [10, 16].

Previous studies of the martensitic transformation in NiTi were performed either along the isothermal or the adiabatic path [3]. In this work, the induced phase transformation proceeds under both adiabatic and isothermal conditions due to the short duration of the experiment (tens of microseconds) and the low equilibrium value of the volume fraction of austenite, respectively.

Multi-frame time-resolved X-ray experiments were performed at the BL40XU beamline at the SPring-8 synchrotron radiation facility (Hyogo, Japan) [15]. The incident X-ray energy was 15.00 keV ($\lambda = 0.8271 \text{ \AA}$), for which the attenuation length in NiTi is approximately 30 μm . Therefore, diffraction was obtained from a thin region with a thickness of approximately 1.1 μm at the periphery of the wire [15].

The XRD beam size captured a segment of 1 mm along the wire axis. Previous studies in Flexinol wires showed that, at the 1 mm length scale, the transformation is uniform along the wire axis [10, 18], i.e., if transformation bands do exist along the wire axis, their size has to be much smaller than 1 mm. Dana et al. [15] performed hundreds of XRD tests at random positions along various wires, obtaining highly repeatable results. Therefore, it is extremely unlikely that their beam probed the fast transformation of a specific band along the wire axis, while other (larger) regions have yet to transform. This conclusion is further supported by the observation that the force sensors located at the two ends of the wire measured the same signal throughout all transformation stages (see detailed discussion in [9]).

The temporal resolution of the collected XRD data (Fig. 3) is approximately 1 μs . This was achieved by combining different sets of experiments conducted under the same conditions with different time delays between the onset of XRD image sampling and that of the heating pulse. Stress measurements throughout these experiments were highly repeatable.

Diffraction Patterns and Intensity Profiles

Figure 1 shows a diffraction ring pattern, taken during the phase transformation, where both the martensite and austenite phases are present. The intensity of martensite reflections associated with different variants strongly depend on the angular coordinate η , in accordance with the average detwinning strain. Two sections of the diffraction rings, shown by the dashed and dotted lines, were chosen for further analysis of diffraction profiles. The intensity profiles shown in Fig. 2 are averaged from two 5° intervals, $0 \leq \eta \leq 5$ and $20 \leq \eta \leq 25$. Due to the fiber texture of the wire, the sampled regions are symmetric across both the y and z axis, amounting to a total of 20 sampled profiles with $d\eta = 1^\circ$. The average projected directions of each interval, representing plane normals with angles of $\Phi \approx 4^\circ$ (red, dashed lines) and $\Phi \approx 23^\circ$ (blue, dotted lines) relative to the wire axis, were calculated using the formulation presented in Ref. [19] for a material with a fiber texture.

Figure 2 presents intensity profiles that were averaged over the two different intervals on the Debye–Scherrer diffraction rings. The diffractograms were obtained at $t = 0$ (dashed curve) and $t = 200 \mu\text{s}$ (solid curve) after the heating pulse. Fig. 2a shows the intensity profile along the direction of the wire ($\Phi \approx 4^\circ$). Initially ($t = 0$), a high intensity peak ($110^M, 020^M$) is evident at a scattering vector value of approximately $q = 2.78 \text{ \AA}^{-1}$ (related to a large positive strain of approximately 6.5%), along with a strong shoulder ($\bar{1}11^M$) at approximately $q = 2.96 \text{ \AA}^{-1}$ (related to approximately zero strain) and a smaller bump ($021^M, 111^M$) near $q = 3.2 \text{ \AA}^{-1}$ (related to large negative strains), see discussion in Ref. [15]. The significant differences in peak intensities are due to the average

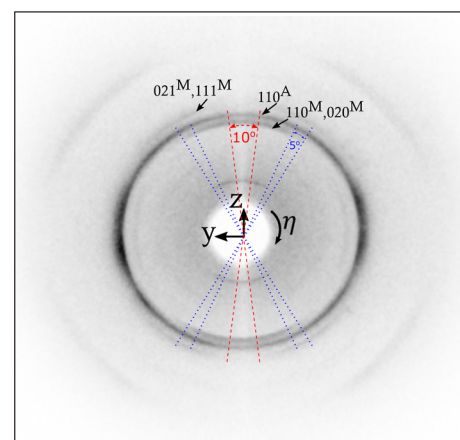


Fig. 1 Debye–Scherrer diffraction pattern, of 1024×1024 pixels, taken at $t = 200 \mu\text{s}$ with an exposure time of 10 μs . The z axis is aligned in the direction of the wire. Several austenite and martensite reflections are marked on the figure. The radius of the 110^A reflection is approximately 2.96 \AA^{-1}

Fig. 2 Intensity profiles vs scattering vector q , taken before the onset of the heating pulse ($t = 0$) and after the transformation reaches equilibrium ($t = 200 \mu\text{s}$, Fig. 1). The profiles were averaged over four symmetric (due to the fiber texture of the wire) 5° intervals along the Debye–Scherrer diffraction ring (see illustration in Fig. 1). **a** $\Phi \approx 4^\circ$. **b** $\Phi \approx 23^\circ$

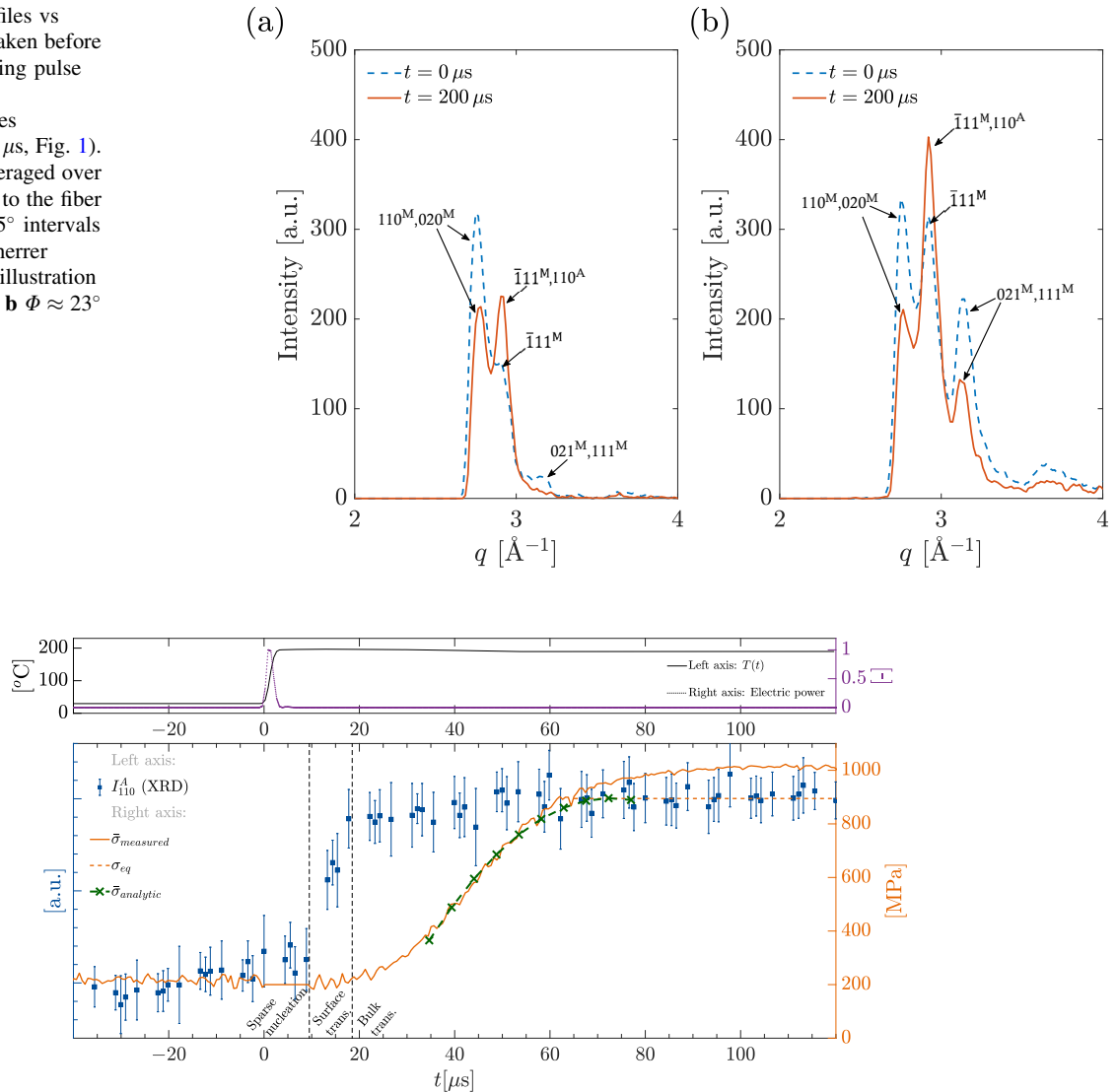


Fig. 3 [Top] Average wire temperature evolution in time, based on Ref. [15]. [Bottom] Experimental results combined from four experiments with varying delays [0, 4.4, 5.5, 6.5] μs . The dotted line shows the $\sim 3 \mu\text{s}$ pulse of electric power transferred to the wire, in normalized units, the onset of the electric pulse was chosen as $t = 0$. The blue squares are the integrated XRD intensity $I^A(t)$ of the austenite peak, normalized with respect to its mean final value (i.e. mean of plateau after 20 μs), corresponding to the estimated 0.261 austenite volume fraction by equation (7). The solid curve is the mean

measured tensile stress from all experiments shown in units of MPa, marked on the right vertical axis. The horizontal dashed line represents the equilibrium stress value averaged azimuthally over the interval [1.4, 5] ms after the pulse. The vertical dashed lines denote the different stages of the transformation. The x-marked dashed line is the analytic solution, Eq. (12), of the tensile stress along the wire based on the proposed kinetic model (discussed in section “Model for a cylindrical phase front”). Reproduced from Dana et al. (2021) [15] with permission from Elsevier

detwinning strain of 0.035 in the direction of the wire, which results in a large amount of the martensitic variant related to the large positive strain. At $t = 200 \mu\text{s}$, the increase of the intensity at $q = 2.96 \text{ \AA}^{-1}$ due to the emerged austenite 110^A peak, is accompanied by a notable decrease in the intensity of the highest martensitic peak along with a proportional decrease of the smaller bump representing the negative strains.

Figure 2b shows the intensity profile along an angle of $\Phi \approx 23^\circ$ from the wire axis. The average longitudinal strain along this direction is smaller, and therefore the intensity of the $110^M, 020^M$ reflections is smaller and that of the $(021^M, 111^M)$ is greater with respect to those presented in Fig. 2a. Here, we see that both sets of reflections decrease by a factor of approximately 1.6, similar to that observed for $110^M, 020^M$ in Fig. 2a. The observed proportionality in the changes of XRD peaks related to

different martensite variants indicates that to a good approximation the average detwinning strain in the martensite phase remained constant at the original value of $\varepsilon_0 = 0.035$. This means that a transformation of a volume fraction x within a given region of the wire results in transformation strain $\varepsilon_{zz}^t = -x\varepsilon_0$ within this region. The transformation strain results in a change of the elastic strain leading to a stress change. Thus, the process probed by the XRD must involve a change in stress.

Time Evolution of XRD Intensities and Force Measurements

The above description of the experimental method can be summarized as follows. The 110^A XRD intensity, measured along the wire axis (similar to Fig. 2a), is proportional to the volume fraction of the austenite within that region, i.e., a layer thickness of approximately $1.1 \mu\text{m}$ near the surface of the wire. At the same time, the average stress, calculated by dividing the measured force by the wire cross sectional area, is a macroscopic measure for the effect of the phase transformation throughout the entire cross section of the wire.

Typical experimental results showing the evolution of the 110^A XRD intensity and stress in the NiTi wire are presented in Fig. 3. In addition, the top panel of the figure shows the power pulse transferred to the wire and the resulting temperature response of the wire (as explained in Ref. [15]). The microsecond-scale time-resolved XRD study of the transformation [15] identified three different stages of the transformation, occurring at different times and length scales.

In the first stage, up to approximately $9 \mu\text{s}$ after the onset of the heating pulse, no detectable response of the wire is observed. Dana et al. [15] assumed that at this stage, sparse nucleation of austenite islands occurs.

The following second stage shows a fast (approximately $9 \mu\text{s}$), steep rise in the volume fraction of the austenite phase near the surface of the wire (blue squares in Fig. 3). Concurrently, the macroscopic stress response (solid curve) during the second stage appears to be negligible. Following the conclusion from section “[Diffraction patterns and intensity profiles](#)” that the strain change probed by the XRD must involve a change in stress, we conclude that the rapid transformation occurs only within a near-surface layer, which is small compared to the total volume of the wire. Furthermore, it is more likely that increased nucleation of austenite will be promoted by the lack of mechanical constraints at the free surface over the highly constrained center. We therefore consider this stage to be the formation of a thin partially transformed martensite-austenite layer near the surface of the wire.

The third, most dominant, stage is the increase of the macroscopic stress (over approximately $30 \mu\text{s}$), signifying the transformation in the bulk of the wire. However, from the end of the second stage ($t \approx 20 \mu\text{s}$), as the transformation evolves ($32 \leq t \leq 65 \mu\text{s}$), the austenite intensity in the region probed by the XRD remains constant at the plateau value. This indicates that a process occurs in the inner part of the wire while the thin outer layer probed by the XRD remains unchanged. The saturation of the diffracted austenite intensity indicates that the volume fraction of austenite within the outer layer reaches an equilibrium value remaining approximately constant throughout the transformation in the bulk. At times $t > 65 \mu\text{s}$, an equilibrium is reached in both the near-surface layer probed by the XRD and the bulk probed by the force sensors.

The effect of the initial stress has been studied in previous work by Vollach et al. [9, 16]. The authors found that the initial stress value does influence the evolved equilibrium stress in the bulk of the wire but barely affects the time required to reach equilibrium.

Theoretical Framework

The observations made in Sect. 2 imply that during the third stage (bulk transformation), the transformation proceeds along the radial direction. This effect may arise due to the high-driving-force conditions or due to the unique boundary conditions imposed in this experiment. At the same time, it should be noted that the common experimental methods used for following the evolution of phase transformations in SMA are based on optical, electron, or IR microscopy, which are mainly sensitive to surface changes. Specifically, previous slow [17, 18] and high [10] rate studies of Flexinol wires measured strain and temperature changes only at the surface and therefore could not observe such effects.

Next, we discuss possible scenarios for the propagation of the phase transformation, in accordance with the obtained experimental results. The studied problem is described using a continuum model at a scale much larger than the grain size ($\sim 100 \text{ nm}$) but much smaller than the wire radius ($100 \mu\text{m}$).

The volume fraction of austenite is described by the general function $x(r, \phi, z, t)$, where r , ϕ and z represent the radial, azimuthal and axial coordinates in a cylindrical system. Due to the cylindrical symmetry of the polycrystalline wire, we assume that x is not a function of ϕ . Furthermore, as discussed in Sect. 2.1, any fluctuations of x as a function of the axial coordinate z , occur at a scale smaller than few tens of μm . For simplicity, we initially assume

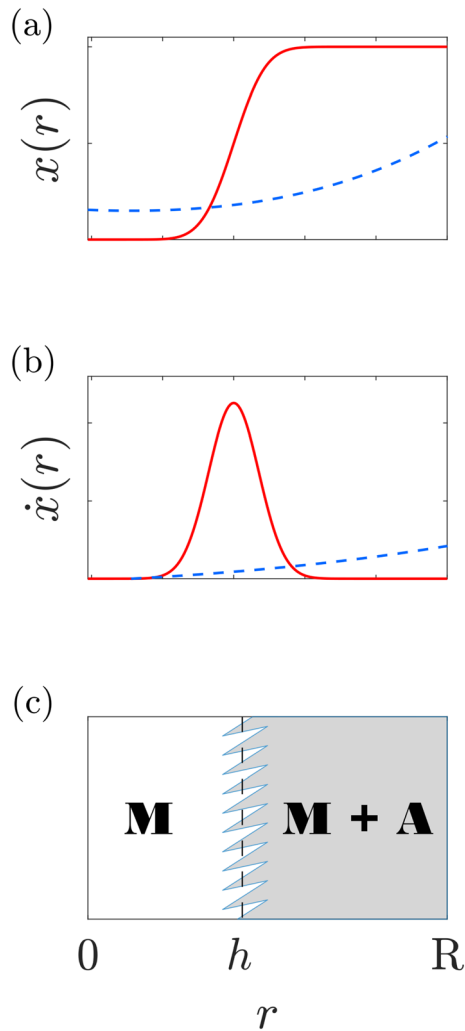


Fig. 4 Schematics of possible shapes of the functions: **a** $x(r)$, and **b** $\dot{x}(r)$, at a given time, t . The solid and dashed lines represent a continuous (e.g., phase front) and gradual spatial distribution of the transformed region, respectively. **c** Illustration of the radial cross section of the wire (in the r - z plane) with a possible boundary between the partially transformed ($M + A$) and untransformed (M) regions in the wire, composed of sharp (needle) interfaces aimed to reduce the misfit strain at the boundary between the different phases (cf. Ref. [4]). If the needles are small enough, they can be considered as a macroscopic front with a rough interface located at the average coordinate h

that x is not a function of z and then elaborate on the issue and soften this ansatz.

Figure 4 presents the schematics of two different possible shapes for the functions $x(r)$ and $\dot{x}(r)$ at a given time, t , where the dot operator is the time derivative. The dashed curves in Fig. 4a and b represent gradual functions describing a situation in which regions at different radial locations have independent transformation rates, i.e., $\dot{x}(r_1) \neq \dot{x}(r_2)$. The solid curves describe a transformation process that takes place via the propagation of a phase front separating the outer partially transformed layer ($M + A$)

from the inner layer that has yet to be transformed (M). Within the region of the phase front, x may vary as a function of z , as illustrated for example in Fig. 4c. Such local variations can reduce the local strain energy [4]. The observation that the austenite volume fraction in the outer region reaches a plateau (equilibrium) value at $t \approx 18 \mu\text{s}$, before the stress begins to rise, deems the scenario described by the dashed curves less probable.

Herein, we introduce a model for the bulk transformation stage ($32 \lesssim t \lesssim 65 \mu\text{s}$ in Fig. 3), during which the stress increases, but the austenite volume fraction within the outer layer has already reached the equilibrium value. For simplicity, we express the function $x(r, t)$ in the form of the step function

$$\begin{cases} x(r, t) = 0, & \text{if } r < R - h(t), \\ x(h), & \text{if } r > R - h(t), \end{cases} \quad (1) \quad (1a) \quad (1b)$$

where $h(t)$ is the thickness of the partially transformed outer layer measured from the wire surface ($r = R$) inward, as depicted in Fig. 5. To consider the evolution of x within this layer, we allow it to change as a function of h . The following model will show that the equilibrium volume fraction of austenite, x_{eq} , is practically insensitive to $h(t)$, in agreement with the observation that $I^A(t)$ remains at a saturated value while $\bar{\sigma}(t)$ increases. The model does not describe the stages at which h or $(R-h)$ are on the scale of a few grains (i.e., smaller than $\sim 1 \mu\text{m}$), in a wire of radius R . Finally, the model will show that although the cylindrical phase front is strain incompatible at the macroscopic scale, the elastic energy due to this strain mismatch is small with respect to the driving force for the phase transformation.

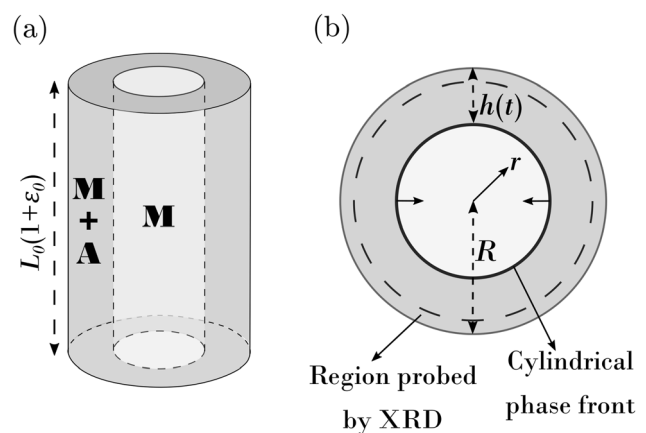


Fig. 5 Schematic illustration of the proposed model for transformation in a wire fixed at both ends with initial length L_0 and transformation strain ϵ_0 . **a** The cylindrical interface, $r = R - h(t)$, between the partially transformed ($M + A$) region and the untransformed (M) region is described by two co-cylindrical bodies in mechanical equilibrium. **b** Cross section of the wire

Model for a Cylindrical Phase Front

This section is organized as follows. We begin by formulating the free energy in the wire and defining the basic conditions at which the transformation occurs. In section “Equilibrium volume fraction of austenite”, we estimate the equilibrium volume fraction of austenite, x_{eq} , in the partially transformed layer. In section “Kinetic-law”, we present a simple kinetic law to account for the velocity of the front and discuss the conditions for its validity. Finally, the obtained model is solved and fitted to the experimental results, providing the kinetic relation between the cylindrical phase front and the driving force propagating it.

The total free energy is expressed by

$$U(h, x) = U(0, 0) - \pi \left(R^2 - (R - h)^2 \right) L x(t) \Delta s \Delta T + \frac{1}{2} \sum_{ij} 2\pi L \int_0^R \sigma_{ij} \varepsilon_{ij} r dr. \tag{2}$$

The first term represents a reference state at which the wire is fully at the martensite phase. The second term represents the reduction of the free energy due to the phase transformation in the outer layer. Here, $L = L_0(1 + \varepsilon_0)$ is the fixed length of the wire, Δs is the entropy change per unit volume and $\Delta T = T - T_0$ is the temperature difference relative to the transformation temperature, T_0 . The third term represents the energy due to the elastic stresses σ_{ij} and strains ε_{ij} . The work of external forces is zero because the wire is clamped at both ends.

Based on the data in Fig. 3, the phase front propagates a distance of 0.1 mm (the wire radius) during approximately 30 μ s. The average phase front velocity of 3.33 m/s is three orders of magnitude smaller than the shear wave speed, $C_T \sim 2000$ m/s. Thus, the stresses in the outer layer (partially transformed region) and the inner core (untransformed region) of the wire can be calculated assuming mechanical equilibrium. The solution to this elastic problem is presented in Appendix A, where all relevant stresses and strains are expressed as functions of $h(t)$ and $x(t)$. For simplicity, we assume that the Young’s moduli and Poisson’s ratios of both the outer layer and the inner core are the same. This assumption is in agreement with ultrasonic

measurements, which showed that at high rates the Young’s moduli of the austenite and martensite phases are approximately the same and are equal to ~ 70 GPa [20].

Equilibrium Volume Fraction of Austenite

We estimate the equilibrium value of the volume fraction, x_{eq} , as a function of the layer thickness, h , by minimizing U , defined in Eq. (2), with respect to x . This procedure, after substituting all of the obtained expressions for σ_{ij} and ε_{ij} from appendix A, provides

$$x_{eq} = \frac{\Delta s \Delta T - \sigma_0 \varepsilon_0}{E \varepsilon_0^2} \left(C_1(\nu) - C_2(\nu) \frac{h(t)}{R} + C_3(\nu) \frac{h^2(t)}{R^2} \right)^{-1}, \tag{3}$$

where E and ν are the Young’s modulus and Poisson’s ratio, and the constants are

$$C_1(\nu) = \frac{(5 - 4\nu)}{4(1 - \nu^2)}, \tag{4a}$$

$$C_2(\nu) = \frac{(1 - 2\nu)^2}{2(1 - \nu^2)}, \tag{4b}$$

$$C_3(\nu) = \frac{(1 - 2\nu)^2}{4(1 - \nu^2)}. \tag{4c}$$

Inspection of Eq. (3) at both limits provides that

$$x_{eq}(h = 0) = \frac{1}{C_1(\nu)} \frac{\Delta s \Delta T - \sigma_0 \varepsilon_0}{E \varepsilon_0^2}, \tag{5}$$

and that

$$x_{eq}(h = R) = \frac{\Delta s \Delta T - \sigma_0 \varepsilon_0}{E \varepsilon_0^2}. \tag{6}$$

A substitution of material properties (listed in Appendix B) into these expressions provides that $x_{eq} \approx 0.261$ (in excellent agreement with previous calculations performed in Ref. [16]) and that the value varies by approximately 3% between the two limits. The latter result validates that x_{eq} is a weak function of $h(t)$, in accordance with our observation that the XRD intensity of the austenite peak remains constant during this stage of the transformation (as shown in Fig. 3).

Table 1 Substituted and calculated model parameters

Parameter	Value	Parameter	Value	Parameter	Value	Parameter	Value
E	70 GPa	σ_0	200 MPa	Δs	0.245 MPa/K	$\frac{(5-4\nu)}{8(1-\nu^2)}$	0.516
ν	0.33	ε_0	0.035	x_{eq}	0.261	a	0.404
ΔT	120 K	h_0	10 μ m	$\frac{\Delta s \Delta T}{E \varepsilon_0^2 x_{eq}}$	1.207	b	0.0649
R	100 μ m	t_0	32 μ s	$\frac{\sigma_0 \varepsilon_0}{E \varepsilon_0^2 x_{eq}}$	0.287	c	- 0.0324

Based on this result, in the following calculation of $h(t)$ we assume a constant value of the austenite volume fraction,

$$x_{eq} \approx \frac{\Delta s \Delta T - \sigma_0 \varepsilon_0}{E \varepsilon_0^2}. \quad (7)$$

The equilibrium values in our experiment, specifically volume fraction, equilibrium stress and temperature, are in agreement with values obtained in a slow-rate study of similar Flexinol wires, see Ref. [17].

Kinetic-Law

The velocity v of the phase front is calculated by assuming a kinetic relation of the form

$$v = \frac{dh(t)}{dt} = \mu_m g, \quad (8)$$

where μ_m is a mobility coefficient, and g is the thermodynamic driving force for the phase transformation defined by

$$g = -\frac{1}{S} \frac{dU}{dh} = -\frac{1}{2\pi(R-h)L} \frac{dU}{dh}, \quad (9)$$

[21]. Here, S is the area of the moving interface (the phase front). The kinetic relation assumed in Eq. (8) describes a motion governed by internal viscosity ($1/\mu_m$). This is typical for cases in which the velocity of the phase front is greater than $10^{-4}C_T$, yet significantly smaller than C_T [22, 23], as in our case.

The substitution of the elastic solution (Appendix A) into equations (2), (9), and (8) yields a linear, first order, ordinary differential equation (see appendix B). Inspection of relative magnitudes of the different terms (Table 1 in appendix B) show that the effect of the mismatch strain energy (third term in Eq. (2)) is approximately 0.43 of the thermally induced contribution to the driving force (second term in Eq. (2)). Substitution of material properties into the obtained expressions shows that the driving force,

$$g \approx 0.5x_{eq}\Delta s\Delta T, \quad (10)$$

and the velocity, v , are approximately constant as a function of h . Thus, h is approximately a linear function of t , i.e.,

$$h(t) \propto \mu_m g t. \quad (11)$$

Finally, the obtained solution for $h(t)$ is substituted into the solution for the mean tensile stress in the wire (see details in Appendix A),

$$\bar{\sigma} = \sigma_0 + E x_{eq} \varepsilon_0 \left(1 - \left(\frac{R-h(t)}{R} \right)^2 \right). \quad (12)$$

A solution of our model (Appendix B) showing the temporal evolution of the mean stress in the wire, is presented by the x-marked dashed line in Fig. 3. An initial condition, $h(t_0) = h_0$, was imposed, where $t_0 = 32 \mu\text{s}$ and $h_0 = 10 \mu\text{m}$ are the time and layer thickness at which the phase front propagation stage begins. The temperature difference is set to $\Delta T = 120 \text{ K}$ (in accordance with the electric energy discharged on the wire), and the only fitted parameter is the mobility of the phase front, μ_m , resulting in the front velocity, $v = \mu_m g = 4 \text{ m/s}$ (see Appendix B for more details), for propagation along the radial coordinate of the wire. The agreement between our model solution for $\bar{\sigma}$ and the measured data further strengthens our analysis.

Conclusions

Our previous results (Ref. [15]) revealed a rapid transformation occurring within a thin layer close to the wire surface, while the bulk of the wire remained untransformed.

This paper focuses on the analysis of the main sub-process that governs the thermo-mechanical response of the wire, during which bulk transformation occurs. Our analysis excludes several mechanisms of transformation propagation, which have been reported to occur at slow rates in different types of samples, and suggests a new mechanism that is in agreement with our experimental observations. In this mechanism, the transformation first occurs at the near-surface layer and then proceeds inward by the propagation of a cylindrical phase front.

We developed a theoretical model for a cylindrical phase front that was fitted to the experimental results and provided a kinetic relation between the velocity of the phase front and the driving force propagating it. The agreement between the fitted model and experimental results further supports our interpretation.

A cylindrical phase front is significantly different than all previously studied transformation phase fronts (see, e.g., Ref. [4]) for it is strain incompatible at the macroscopic scale. That is, the misfit strains at the phase front induce internal stresses throughout the entire volume of the wire and increase the elastic strain energy. On the other hand, the cylindrical phase front is formed more easily due to the lack of mechanical constraints at the surface. To complete the transformation, the phase front has to propagate just 0.1 mm (~ 500 times smaller than the length of the wire). Broadly speaking, the transformation mechanism at large driving force values implies the releasing of the excess energy as fast as possible, rather than following the minimal energy path. This behavior resembles crack propagation dynamics in the large driving force regime, e.g., [24],

and is reasoned to be a result of the conditions at which the thermally induced driving force is much larger than the effect of the energy due to misfit strains.

The obtained results reveal several interesting insights. First, the velocity of the proposed phase front (about 4 m/s) is much smaller than the shear wave speed ($\sim 2000\text{m/s}$), suggested as an estimation for the velocity of austenite–martensite interfaces in ideal single crystals [25]. Second, the extracted kinetic relation in equation (8) describes an irreversible thermodynamic process governed by viscous resistance. Third, the slow phase front velocity is due to the relatively small value of the mobility coefficient μ_m , inversely proportional to the viscous resistance. The latter is predominantly higher in strain incompatible phase fronts due to the associated stress changes in the entire volume of the material.

Future work should include the use of a high energy ($> 20\text{ keV}$) x-ray beam to overcome beam attenuation in the material, enabling measurements at varying locations along the wire cross-section.

Acknowledgements The research is supported by Israel Science Foundation (Grant No. 1309/18) and Technion-GTIIT startup grant. The time-resolved diffraction experiment were performed at BL40XU/SPring-8 with the approval of the Japan Synchrotron Radiation Research Institute (Proposal No. 2018B1398).

Declarations

Conflict of interest The authors declare that they have no conflict of interest.

Appendix 1: Elastic Problem

Herein, we formulate and solve the boundary value problem related to the stress and strain tensors in a wire that consists of an untransformed martensite cylindrical core surrounded by a partially transformed cylindrical shell with a thickness h and an austenite volume fraction x . For simplicity, we ignore any preferred crystallographic orientation along the wire axis and assume that both the core and the shell can be described as isotropic materials with a Young’s modulus E and a Poisson’s ration ν . Moreover, based on previous ultrasonic measurements [20, 26], we assume that at the high rates relevant for this study E and ν of the austenite and martensite phases have the same values. As discussed above, $\dot{h} \ll C_T$, therefore the elastic problem is solved under the assumption of force equilibrium.

Initially, three superscripts are defined: c -core (untransformed martensite core), s -shell (partially transformed austenite shell), t -transformation. We follow Ref. [27], p. 124, which solves the equilibrium problem of

axisymmetric co-cylinders. The governing equilibrium equation is formulated, for each of the materials, in terms of their radial displacement, u_r , to obtain

$$\frac{d^2 u_r}{dr^2} + \frac{1}{r} \frac{du_r}{dr} - \frac{u_r}{r^2} = 0, \tag{13}$$

which has the solution

$$u_r(r) = \begin{cases} A^c r, & 0 \leq r \leq R - h(t), \\ A^s r + B^s / r, & R - h(t) \leq r \leq R. \end{cases} \tag{14}$$

The boundary conditions for the problem are

$$u_r^c(R - h(t)) = u_r^s(R - h(t)), \tag{15}$$

$$\sigma_{rr}^c(R - h(t)) = \sigma_{rr}^s(R - h(t)), \tag{16}$$

$$\sigma_{rr}^s(R) = 0. \tag{17}$$

The conditions specified in Eqs. (15) and (16) represent continuity of displacement and stress at the interface, Eq. (17) specifies zero constraints on the outer surface of the wire (free surface).

We formulate the elastic relations between the stresses and the elastic strains for both the core and the shell,

$$\begin{bmatrix} \sigma_{rr}^c \\ \sigma_{\theta\theta}^c \\ \sigma_{zz}^c \end{bmatrix} = \frac{E}{(1 + \nu)(1 - 2\nu)} \begin{bmatrix} 1 - \nu & \nu & \nu \\ \nu & 1 - \nu & \nu \\ \nu & \nu & 1 - \nu \end{bmatrix} \begin{bmatrix} \epsilon_{rr}^c \\ \epsilon_{\theta\theta}^c \\ \epsilon_{zz}^c \end{bmatrix}, \tag{18a}$$

$$\begin{bmatrix} \sigma_{rr}^s \\ \sigma_{\theta\theta}^s \\ \sigma_{zz}^s \end{bmatrix} = \frac{E}{(1 + \nu)(1 - 2\nu)} \begin{bmatrix} 1 - \nu & \nu & \nu \\ \nu & 1 - \nu & \nu \\ \nu & \nu & 1 - \nu \end{bmatrix} \begin{bmatrix} \epsilon_{rr}^s \\ \epsilon_{\theta\theta}^s \\ \epsilon_{zz}^s \end{bmatrix}. \tag{18b}$$

The total strains in the outer shell (in all three directions) are each comprised a transformation component and an elastic contribution such that

$$\epsilon_{kk}^{s,total} = \epsilon_{kk}^s + \epsilon_{kk}^t, \tag{19}$$

where the index k represents each of the coordinates (r, θ, z) . Concurrently, phase transformation has not yet occurred in the inner core and therefore its total strain is purely elastic. The strain due to transformation in the direction of the wire is $\epsilon_{zz}^t = -\epsilon_0 x$, where x is the volume fraction of austenite in the wire, as described in the main text. Also, since the wire is fixed at both ends, $\epsilon_{zz}^{c,total} = \epsilon_{zz}^{s,total} = \sigma_0/E$, where σ_0 is the initial stress in the wire that is applied before the heat pulse. We thus obtain that $\epsilon_{zz}^s = \sigma_0/E + \epsilon_0 x$. Due to volume conservation of the transformation strains,

$$\epsilon_{rr}^t + \epsilon_{zz}^t + \epsilon_{\theta\theta}^t = 0, \tag{20}$$

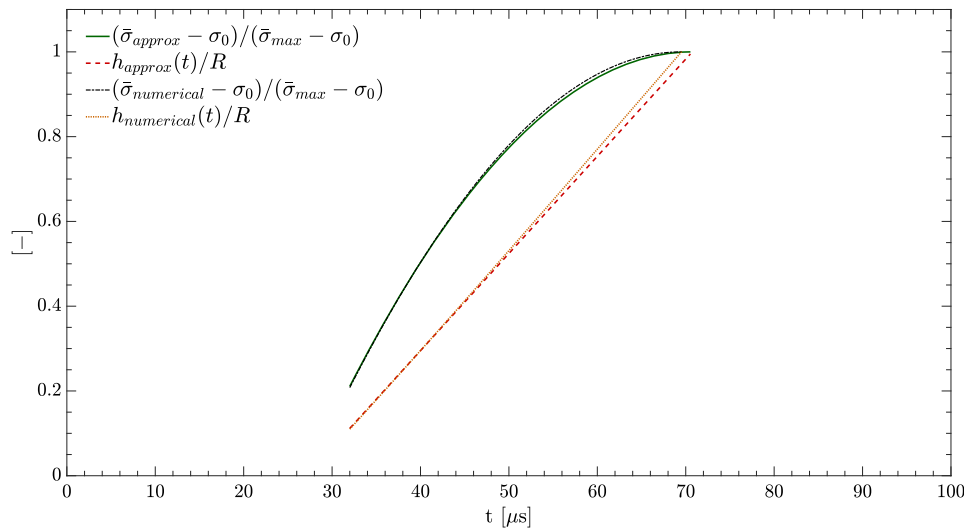


Fig. 6 Solutions to the proposed kinetic model, Eq. (23). The analytic approximate linear solution, h_{approx} (neglecting the second and third terms on the RHS), is compared to a full numerical calculation, $h_{numerical}$. The normalized temporal evolution of the front location with respect to the radius of the wire, $h(t)/R$, is presented in the dashed

(approximate solution) and dotted (full numerical solution) lines. The mean stress (solid, approximate solution and dash-dotted, full numerical solution) in the wire is normalized relative to its maximum value (obtained at $h = 1$), i.e., $\bar{\sigma}/\bar{\sigma}_{max}$, with the maximum obtained value $\bar{\sigma}_{max} \approx 0.9$ GPa

leading to $\epsilon_{rr}^t = \epsilon_{\theta\theta}^t = \frac{1}{2} \epsilon_0 x$.

Substituting Eq. (13) into the strain-displacement relations, $\epsilon_{\theta\theta} = u_r/r$ and $\epsilon_{rr} = du_r/dr$, and combining with Eqs. (18) and (19), we obtain expressions for the elastic strains in terms of the constants, A^c , A^s , and B^s . Then, substituting the results into boundary conditions (15), (16), and (17), we obtain the solution

$$A^c = \frac{x\epsilon_0(1-2\nu)^2}{4(1-\nu)} \frac{(R^2 - (R-h)^2)}{R^2} - \frac{\nu\sigma_0}{E}, \tag{21a}$$

$$A^s = \frac{x\epsilon_0(1-2\nu)}{2} - \frac{x\epsilon_0(1-2\nu)^2}{4(1-\nu)} \frac{(R-h)^2}{R^2} - \frac{\nu\sigma_0}{E}, \tag{21b}$$

$$B^s = -\frac{x\epsilon_0(1-2\nu)(R-h)^2}{4(1-\nu)}, \tag{21c}$$

which can then be used to express all of the elastic strains and stresses. Finally, we calculate the mean longitudinal stress in the z direction,

$$\begin{aligned} \bar{\sigma} &= \frac{2\pi \int_0^{R-h(t)} \sigma_{zz}^c r dr + 2\pi \int_{R-h(t)}^R \sigma_{zz}^s r dr}{\pi R^2} \\ &= \sigma_0 + Ex\epsilon_0 \left(1 - \left(\frac{R-h(t)}{R} \right)^2 \right). \end{aligned} \tag{22}$$

The solution for the evolution of the thickness of the outer shell, $h(t)$, is then substituted into equation (22), and both curves are presented in Fig. 6 (see Appendix 2).

Appendix 2: Kinetic Model

The substitution of the above solution for the elastic problem into the kinetic law in Eq. (8) in the main text yields the linear, first order ODE,

$$\dot{h} = \tilde{\mu}_m \left(a + b \frac{h}{R} + c \frac{h^2}{R^2} \right), \tag{23}$$

where the modified mobility parameter, $\tilde{\mu}_m$ (in units of m/s), obeys the relation

$$\tilde{\mu}_m = \mu_m \left(E\epsilon_0^2 x_{eq}^2 \right), \tag{24}$$

and the constants are accordingly

$$a = \frac{\Delta s \Delta T}{E\epsilon_0^2 x_{eq}} - \frac{\sigma_0 \epsilon_0}{E\epsilon_0^2 x_{eq}} - \frac{(5-4\nu)}{8(1-\nu^2)}, \tag{25a}$$

$$b = \frac{(1-2\nu)^2}{2(1-\nu^2)}, \tag{25b}$$

$$c = -\frac{(1-2\nu)^2}{4(1-\nu^2)}. \tag{25c}$$

Additionally, the initial condition, $h(t_0) = h_0$, was imposed, where t_0 and h_0 are the time and layer thickness at which the phase front propagation stage begins.

The RHS of the obtained ODE (23) is a second degree polynomial, which has an analytic solution. Nonetheless, an inspection of the magnitudes of the constants b and c (Table 1) showed that their respective terms are negligible throughout the solution, i.e., $0 \leq h(t) \leq R$. Thus, the RHS collapses to the constant $\tilde{\mu}_m a$, corresponding with a

constant driving force for the transformation and thus a constant front velocity resulting in a linear profile for $h(t)$ (Eq. (11) in the main text). A closer estimation of the magnitudes of the different terms in a (Table 1) shows that since the effect of the initial stress, σ_0 , is small, the driving force is dominated by the thermodynamic heating term $\Delta s \Delta T$ and that the resulting driving force can be approximated to the expression $g \approx 0.5x_{eq} \Delta s \Delta T$.

The parameters that were substituted into the model (see Table 1) generally follow those estimated in Ref. [9]. The temperature difference was set as $\Delta T = 120$ K, which implies a wire temperature of approximately 473 K (200 °C) and the total entropy change was estimated as the slope of a specialized Clausius–Clapeyron equation for uniaxial stress, i.e., the linear slope of the equilibrium stress vs. the wire temperature, $\Delta s \approx (7\varepsilon_0)$ MPa/K, cf. Ref. [16]. The mobility parameter, $\tilde{\mu}_m = 4$ m/s, was fitted for the solution that was obtained by imposing the initial condition, $h_0 = 10 \mu\text{m}$ and $t_0 = 32 \mu\text{s}$, to agree with the experimental results.

The solution for the model presented in Fig. 3 is the linear analytic solution for the simplified Eq. (23) (i.e., with the 2nd and 3rd terms neglected). The solution was compared to a numerical calculation that included all three terms of the RHS, which was found to be in good agreement throughout the range of the solution, i.e., $0 \leq h(t) \leq R$, in Fig. 6, where the time evolutions of both solutions are compared. The normalized front location, $h(t)/R$, is presented by the dashed (linear approximate solution) and dotted (full numerical) lines, and the mean tensile stress, $(\bar{\sigma} - \sigma_0)/(\sigma_{max} - \sigma_0)$ is presented by the solid (linear approximate solution) and dash-dotted (full numerical) lines.

References

- Porter DA, Easterling KE, Sherif M (2009) Phase transformations in metals and alloys, (revised reprint). CRC Press, Boca Raton
- Christian JW (2002) The theory of transformations in metals and alloys. Newnes, London
- Li M, Chen M, Sun QP (2020) Nonlocal modeling and analysis of spatiotemporal patterns in non-isothermal phase transformation of NiTi strips. *Int J Solids Struct* 221:103–116
- Dong L, Zhou R, Wang X, Hu G, Sun QP (2016) On interfacial energy of macroscopic domains in polycrystalline NiTi shape memory alloys. *Int J Solids Struct* 80:445–455
- Kim K, Daly S (2011) Martensite strain memory in the shape memory alloy nickel-titanium under mechanical cycling. *Exp Mech* 51(4):641–652
- Escobar J, Clifton R (1995) Pressure-shear impact-induced phase transformations in cu-14.44 al-4.19 ni single crystals. In: Active materials and smart structures, vol. 2427. International Society for Optics and Photonics, pp. 186–197
- Nemat-Nasser S, Choi J, Guo W, Isaacs J (2005) Very high strain-rate response of a niti shape-memory alloy. *Mech Mater* 37(2–3):287–298
- Niemczura J, Ravi-Chandar K (2006) Dynamics of propagating phase boundaries in niti. *J Mech Phys Solids* 54(10):2136–2161
- Vollach S, Shlagman H, Shilo D (2017) Kinetics of the reverse martensitic transformation in shape memory alloys under an abrupt heating pulse. *Scripta Mater* 135:76–79
- Vollach S, Shilo D, Shlagman H (2016) Mechanical response of shape memory alloys under a rapid heating pulse-part II. *Exp Mech* 56(8):1465–1475
- Vollach S, Shilo D (2010) The mechanical response of shape memory alloys under a rapid heating pulse. *Exp Mech* 50(6):803–811
- Ichiyanagi K, Takagi S, Kawai N, Fukaya R, Nozawa S, Nakamura KG, Liss KD, Kimura M, Si A (2019) Microstructural deformation process of shock-compressed polycrystalline aluminum. *Sci Rep* 9(1):7604
- Meredith CS, Herl Z, Young ML (2019) Mechanical behavior and deformation mechanisms of mg-based alloys in shear using in-situ synchrotron radiation x-ray diffraction. In: Dynamic behavior of materials, vol 1. Springer, pp. 283–296
- Lambert P, Hustedt C, Vecchio K, Huskins E, Casem D, Gruner S, Tate M, Philipp H, Woll A, Purohit P et al (2014) Time-resolved X-ray diffraction techniques for bulk polycrystalline materials under dynamic loading. *Rev Sci Instrum* 85(9):093901
- Dana A, Sekiguchi H, Aoyama K, Faran E, Liss KD, Shilo D (2021) The evolution of the martensitic transformation at the high-driving-force regime: a microsecond-scale time-resolved x-ray diffraction study. *J Alloy Compd* 856:157968
- Vollach S, Caciularu R, Shilo D (2017) Equilibrium stress during the response of shape memory alloys to an abrupt heat pulse. *Scripta Mater* 141:50–53
- Šittner P, Sedlák P, Seiner H, Sedmák P, Pilch J, Delville R, Heller L, Kadeřávek L (2018) On the coupling between martensitic transformation and plasticity in niti: experiments and continuum based modelling. *Prog Mater Sci* 98:249–298
- Reedlunn B, Daly S, Hector L, Zavattieri P, Shaw J (2013) Tips and tricks for characterizing shape memory wire part 5: full-field strain measurement by digital image correlation. *Exp Tech* 37(3):62–78
- Cullity B, Stock S (2014) Elements of X-ray diffraction. Pearson Education, London
- Thomasová M, Sedlák P, Seiner H, Janovská M, Kabla M, Shilo D, Landa M (2015) Young's moduli of sputter-deposited NiTi films determined by resonant ultrasound spectroscopy: austenite, r-phase, and martensite. *Scripta Mater* 101:24–27
- Abeyaratne R, Knowles JK (2006) Evolution of phase transitions: a continuum theory. Cambridge University Press, Cambridge
- Faran E, Shilo D (2013) The kinetic relation for twin wall motion in nimga-part 2. *J Mech Phys Solids* 61(3):726–741
- Daphalapurkar N, Wilkerson J, Wright T, Ramesh K (2014) Kinetics of a fast moving twin boundary in nickel. *Acta Mater* 68:82–92
- Cramer T, Wanner A, Gumbsch P (2000) Energy dissipation and path instabilities in dynamic fracture of silicon single crystals. *Phys Rev Lett* 85(4):788
- Zhen Y, Vainchtein A (2008) Dynamics of steps along a martensitic phase boundary I: semi-analytical solution. *J Mech Phys Solids* 56(2):496–520
- Šittner P, Landa M, Lukáš P, Novák V (2006) R-phase transformation phenomena in thermomechanically loaded niti polycrystals. *Mech Mater* 38(5–6):475–492
- Hyer MW, White SR (2009) *Stress analysis of fiber-reinforced composite materials*. DESTech Publications, Inc

Publisher's Note Springer Nature remains neutral with regard to jurisdictional claims in published maps and institutional affiliations.